Computing the Reconnection Rate in Turbulent Kinetic Layers by using Electron Mixing to Identify Topology

W. Daughton and T.K.M. Nakamura

Los Alamos National Laboratory, Los Alamos, NM 87545

H. Karimabadi

Department of Electrical and Computer Engineering, UCSD, La Jolla, CA 92093 and

SciberQuest, Inc., Del Mar, CA 92014

V. Roytershteyn

SciberQuest, Inc., Del Mar, CA 92014

B. Loring

Lawrence Berkeley National Laboratory, Berkeley, CA 94720
(Dated: February 24, 2014)

Three-dimensional kinetic simulations of magnetic reconnection for parameter regimes relevant to the magnetopause current layer feature the development of turbulence, driven by the magnetic and velocity shear, and dominated by coherent structures including flux ropes, current sheets and flow vortices. Here we propose a new approach for computing the global reconnection rate in the presence of this complexity. The mixing of electrons originating from separate sides of the magnetopause layer are used as a proxy to rapidly identify the magnetic topology, and thus track the evolution of magnetic flux. The details of this method are illustrated for an asymmetric current layer relevant to the subsolar region and for a flow shear dominated layer relevant to the lower lattitude magnetopause. While the three-dimensional reconnection rates show a number of interesting differences relative to the corresponding two-dimensional simulations, the time scale for the energy conversion remains very similar. These results suggest that the mixing of field lines between topologies is more easily influenced by kinetic turbulence than the physics responsible for the energy conversion.

PACS numbers:

I. INTRODUCTION

Magnetic reconnection remains one of the most widespread and challenging problems in plasma physics, due to the inherent cross-scale coupling ranging from global structures down to the ion and electron kinetic scales. The energy conversion and plasma transport arising from reconnection are believed to be of key importance in fusion machines, planetary magnetospheres, the solar corona, and a variety of astrophysical applications. Within two-dimensional (2D) models, the basic understanding of how reconnection proceeds in both collisional and kinetic parameter regimes has progressed rapidly in recent years (e.g., see [1–3] and references therein). In comparison, the influence of realistic three-dimensional (3D) dynamics in large systems remains far less explored. To begin with, defining and computing the 3D reconnection rate is much more difficult in magnetic geometries that are intrinsically three-dimensional (e.g. see [4] and references therein). In addition, researchers have suggested that reconnection may be quite different in in large astrophysical problems due to pre-existing turbulence [5–11], or field line chaos [12–15].

From a computational perspective, progress in understanding the 3D evolution of reconnection has been severely constrained due to the inherent multi-scale nature of the problem. This is particularly true for fully kinetic simulations, which offer a rigorous description of collisionless reconnection but at the expense of resolving electron spatial and temporal scales. However, the recent advent of petascale computing has greatly expanded the range of problems which are now feasible with 3D simulations [16]. These capabilities are particularly relevant to the Earth's magnetosphere, where reconnection is known to occur within thin current layers approaching the ion inertial scale (see review in Ref. [17]). Interest in understanding reconnection physics in these collisionless regimes is further motivated by the upcoming Magnetospheric Multi-Scale (MMS) mission, which will provide high-resolution measurements of reconnection layers down to the electron kinetic scales [18]. During the first year, the orbit will be optimal for studying reconnection at the magnetopause, a current layer separating the shocked solar wind from the magnetosphere. The rotation angle of the magnetic field across the magnetopause varies widely, and is often significantly less than 180°. Along the magnetopause, there are several mechanisms that can drive strong turbulence. First, in these guide field geometries the tearing instability is potentially unstable at multiple resonance surfaces across the initial layer [19] corresponding to oblique angles relative to 2D models which permit only a single resonance surface. In recent large-scale 3D kinetic simulations, this was shown to result in a spectrum of interacting flux ropes, both within the initial current layer and nonlinearly within electron-scale current layers that form along separatrices [20, 21]. The continual formation and interaction of these structures give rise to turbulence, which is multi-fractal [22] and dominated by coherent structures including flux ropes and current sheets. While these predictions are still fairly new, observational evidence has been reported for small-scale flux ropes along the edge of the reconnection jet [23] and multi-fractal turbulence in reconnection outflows [24]. Second, in the lower-latitude regions of the magnetopause boundary, strong shear flows can drive the Kelvin-Helmholtz (KH) instability leading to the wrap-up and compression of the current layer. This can drive reconnection along regions of the magnetopause where it would not occur otherwise. Large-scale 3D kinetic simulations have demonstrated these compressed regions are unstable to the formation of numerous small-scale flux ropes in agreement with recent spacecraft observations [25]. Over longer time scales, this so-called *vortex-induced* reconnection gives rise to a strongly turbulent boundary layer with a multitude of embedded electron inertial scale current layers.

These recent simulations demonstrate that the development of 3D reconnection within ion-scale current layers will spontaneously generate turbulence with multiple interacting reconnection sites. Defining and computing the global reconnection rate in the presence of this 3D complexity has posed a significant challenge. While in 2D models, the magnetic topology and corresponding reconnection rate are easily computed through the flux function, the generalization of these ideas to compute 3D reconnection rates remains an area of active research. One straightforward practical approach is to simply evaluate the inflow velocity of plasma into the main reconnection site [26]. This method is appealing since it can even be applied to spacecraft observations [17]. However, this approach is only strictly valid for a single steady-state reconnection site with well-defined inflow and outflow regions. When there are many interacting reconnection sites, or if the reconnection geometry deviates from the simple 2D picture, this approach is unworkable.

Within global magnetospheric geometry, a number of approaches have been developed [27–29] to identify magnetic separators - a magnetic field line connecting two nulls and separating regions of different topologies. The global reconnection rate then corresponds to the line integral of the parallel electric field $E_\parallel$ along this separator [30]. However, in local simulations of the magnetopause boundary, it is not yet clear how to apply these approaches. This is especially true for the general case with ambient guide field which lacks magnetic nulls. In this limit, the mapping of field lines across the system is continuous, and true topological separatrices do not exist [31]. Nevertheless, neighboring magnetic field lines diverge very rapidly in certain regions as measured by the so-called squashing factor [32–34], or the closely related Lyapunov exponent [14, 35, 36]. Recently, a method has been proposed for computing the reconnection rate in this limit based on a generalized flux function [13], but so far the method has only been applied to line-tied boundary conditions.

Another general approach for computing the 3D rate involves integrating the parallel electric field $E_\parallel$ along all field lines to compute the quasi-potential [37]. Applying this approach to recent large-scale kinetic simulations, the largest values of the quasi-potential are well correlated with the squashing factor [38], and the inferred reconnection rates [21, 38] are comparable to corresponding 2D simulations. While these initial efforts are promising, there remains some ambiguity regarding the field line integration of $E_\parallel$ for these kinetic simulations. As originally formulated [37], the integration should proceed through a non-ideal region back into an ideal region ($E_\parallel = 0$), which is very difficult to identity due to persistent temperature anisotropy in these collisionless layers [39]. For simulations with open boundary conditions [38] it seems reasonable to follow the integration until a field line hits a boundary. However, for doubly periodic simulations the field lines appear to be chaotic within the reconnection layer [21]. If there are special closed fields lines embedded in this chaos, new algorithms would be needed to identify and track the integrated $E_\parallel$ along these closed lines. In either case, field line integrations for the entire volume are very expensive. In order to understand the differences between 2D and 3D reconnection, it is crucial to accurately compute the time evolving reconnection rate in a manner that is practical and robust for large systems.

With this goal in mind, we propose an alternative method to compute the global 3D reconnection rate by using particle mixing as a proxy to identify the distinct magnetic topologies. These regions are bounded by *separatrix surfaces* - corresponding to the surface of field lines that encompass flux from a single source [40]. Although these separatrix surfaces can be identified by field line integration through the volume, this quickly becomes very expensive for large systems. Instead, to rapidly identify these boundaries we exploit the connection between the magnetic topology and the mixing of particles that originate from separate sides of the current layer. Physically, this implies that the particle mixing occurs primarily through the rapid parallel streaming along newly reconnected field lines. While in principle one would use either electrons or ions, physically one would expect this approximation to hold much better for the electrons due to their small gyoradius and rapid thermal motion. Of course, as a final sanity check one can always revert back to magnetic field line integration to determine the separatrix surfaces. However, for the cases presented in this manuscript, we demonstrate that the mixing approach accurately identifies the separatrix surfaces, thus allowing us to compute the time-evolving reconnection rate in a defensible manner.

In this manuscript, we illustrate this approach for two of our largest 3D fully kinetic simulations performed with the particle-in-cell code VPIC which has been carefully optimized for petascale architectures [16]. These examples include an asymmetric current layer relevant to subsolar magnetopause and a current layer with Alfvénic velocity shear relevant to the lower-latitude magnetopause.

II. ASYMMETRIC LAYER

At the subsolar magnetopause, observations suggest [18] that the current layer is reasonably well approximated by an asymmetric generalization of the well-known Harris equilibrium [41]. Here we employ a form which has been used recently to study kinetic instabilities at the magnetopause [42, 43]. Although not an exact Vlasov equilibrium, the plasma is in force-balance across the layer and in the absence of instabilities quickly relaxes to a kinetic equilibrium.

A. Simulation Setup

The initial magnetic field profile is of the form

$$\mathbf{B}(z) = \left[\frac{(B_1 - B_0)}{2} + \frac{(B_0 + B_1)}{2}\tanh\left(\frac{z}{\lambda}\right)\right]\hat{\mathbf{x}} + B_y\hat{\mathbf{y}} \ ,$$

where B_0 is the asymptotic field in the magnetosheath (bottom), B_1 is the magnetic field on the magnetospheric side (top), λ is the half-thickness of the layer and B_y is a spatially uniform guide field. The equilibrium is supported by two components with total density $n(z) = n_h(z) + n_b(z)$. The current is carried by a Harris-like component with density $n_h(z) = n_c \tanh(z/\lambda)$ where n_c is density at the center of the layer. The initial distributions are Maxwellian with spatially uniform drift velocity $U_{ys} = 2cT_s/(q_s B_h \lambda)$, where $B_h \equiv (B_0 + B_1)/2$ and uniform initial temperature T_s for both species ($s = i, e$). Pressure balance requires $B_h^2 = 8\pi n_c(T_i + T_e)$ and the resulting current density is $J_y = J_c \ \mathrm{sech}^2(z/\lambda)$ where $J_c = cB_h/(4\pi\lambda)$. The second component is a non-drifting Maxwellian with density

$$n_b(z) = \frac{(n_1 + n_0)}{2} + \frac{(n_1 - n_0)}{2}\tanh\left(\frac{z}{\lambda}\right) \ ,$$

where n_0 is the density in the magneosheath (bottom) and n_1 is the density in the magnetosphere (top). The ion and electron temperatures are equal to the Harris component. For normalization purposes, we employ the reference parameters on the high-density magnetosheath side of the layer. Thus spatial scales are normalized by the inertial length $d_s \equiv c/\omega_{ps}$ for each species where $\omega_{ps} = (4\pi n_0 e^2/m_s)^{1/2}$ and time is normalized by the cyclotron frequency $\Omega_{cs} = eB_0/(m_s c)$.

For this simulation, the system size is $L_x \times L_y \times L_z = 85d_i \times 85d_i \times 35d_i$ with $2920 \times 2920 \times 1200$ cells and a total of 2×10^{12} computational particles. The half-thickness of the initial current is $\lambda = d_i$, and the density change across the layer is $n_1/n_0 = 0.125$. In the magnetosheath, we choose $\beta_{x0} = 8\pi n_0(T_i + T_e)/B_0^2 = 1$, which through force-balance implies $\beta_{x1} = 0.067$. With these choices, the change in the reconnecting component of magnetic field across the layer is

$$\frac{B_1}{B_0} = \left[1 + \beta_0\left(1 - \frac{n_1}{n_0}\right)\right]^{1/2} \approx 1.37 \ .$$

The ion to electron mass ratio is $m_i/m_e = 100$ with temperature ratio $T_i/T_e = 2$. The ratio of the plasma frequency to electron cyclotron frequency is $\omega_{pe}/\Omega_{ce} = 2$ and the thermal speed is $v_{the} = \sqrt{T_e/m_e} \approx 0.2c$. The boundary conditions are periodic in the x and y directions, while on the z-boundaries particles are reflected and the field boundary conditions are conducting. To initiate reconnection in a controlled manner, a magnetic perturbation of the form

$$\begin{aligned}
\delta B_x &= -\frac{\epsilon}{2}\left(\frac{L_x}{L_z}\right)\cos\left[\frac{2\pi(x - 0.5L_x)}{L_x}\right]\sin\left(\frac{\pi z}{wL_z}\right) , \\
\delta B_z &= \epsilon \sin\left[\frac{2\pi(x - 0.5L_x)}{L_x}\right]\cos\left(\frac{\pi z}{L_z}\right) ,
\end{aligned}$$

is imposed with $\epsilon = 0.03B_o$.

In order to track mixing, the particles are tagged based on which side of the layer they originate. Magnetospheric particles with initial position $z > 0$ are designated as the *top* population, while magnetosheath particles with initial $z < 0$ are the *bottom* population. At any later time, the velocity space moments can be computed separately for each of these groups, as for example, the electron density of the top n_e^{top} or bottom n_e^{bot}. As reconnection develops, these populations will interpenetrate and we can define an electron mixing fraction within each cell

$$\mathcal{F}_e = \frac{n_e^{bot} - n_e^{top}}{n_e^{bot} + n_e^{top}} \ , \tag{1}$$

which will vary continuously from $\mathcal{F}_e = -1$ in regions of pure magnetospheric plasma to $\mathcal{F}_e = 1$ in regions of pure magnetosheath plasma.

B. Results

The time evolution of the current density is shown in Fig. 1 for a 2D slice in the x-z plane at $y = 0$. Streamlines of the in-plane ion flow velocity are shown as white lines,

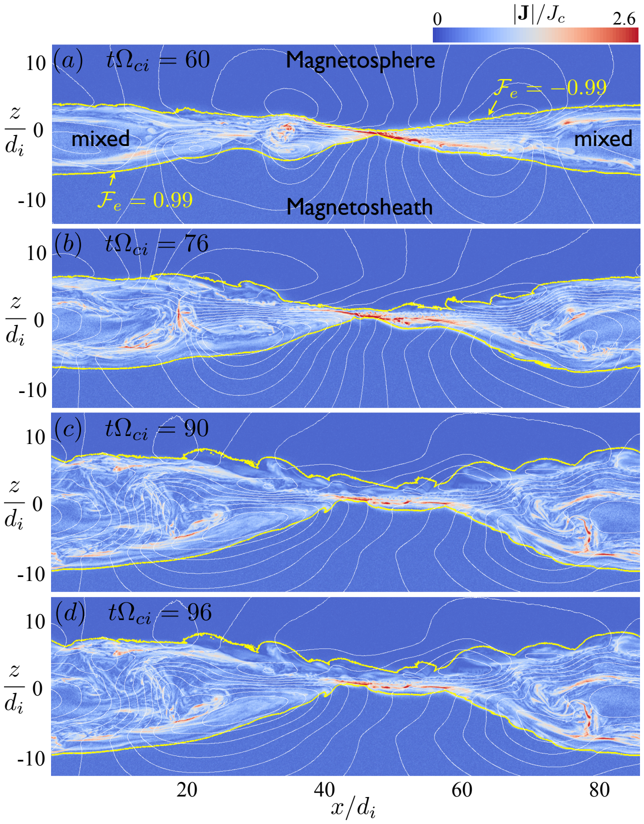

FIG. 1: Time evolution of the current density for an x-z plane at $y = 0$. The white lines correspond to the in-plane streamlines for the ion flow velocity while the yellow lines correspond to contours of the mixing fraction $\mathcal{F}_e$ as indicated. The current density is normalized by $J_c = cB_h/(4\pi\lambda)$.

and two selected contours of the electron mixing fraction are shown in yellow. Physically, these contours correspond to cells where approximately one percent of the particles originated from the opposite side of the layer. The plasma above the $\mathcal{F}_e = -0.99$ contour is purely of purely magnetospheric origin, while the plasma below the $\mathcal{F}_e = 0.99$ contour is purely from the magnetosheath side. As we will demonstrate later, the precise value of these contours is not too important, since gradient in the mixing fraction is extremely sharp along these boundaries. Within 2D simulations, these simple thresholds on the electron mixing fraction are nearly perfect markers of the separatrices identified rigorously from the flux function (i.e., the out-of-plane component of the vector potential A_y). Assuming that streaming along reconnected field lines remains the dominant mixing mechanism, one would expect this approach to identify separatrix surfaces in 3D.

Notice that at early time in Fig. 1a, the current density is primarily concentrated in the center of the box where the yellow contours nearly meet at an apparent separator (i.e., the intersection of two separatrix surfaces). The ion flow is coming into this region from the top and bottom and exiting to the left and right in Alfvénic outflow jets. At this time, the structure is quite similar to the corresponding 2D simulation (not shown). As the evolution proceeds, the diffusion region current sheet expands and fragments into filaments (see panel b), which we will show correspond to flux ropes. In addition, many current sheets form in the outflow with characteristic thickness on the electron inertial scale. At still later time Figs. 1c-d, additional structures associated with the turbulence form along the magnetospheric side of the layer. These are likely driven by the counter-streaming flow from the reconnection jets that arises due to the periodic boundary conditions. As a result of this turbulence, the yellow mixing contours are well separated throughout the volume starting for simulation times $t\Omega_{ci} \gtrsim 70$. This implies that the separatrix surfaces no longer intersect along a single line. At these late times, the flow pattern from the bottom side into the central diffusion region remains coherent and well directed, while the flow pattern on top side of the layer is irregular and dispersed.

The three-dimensional structure for this simulation is illustrated in Fig. 2 at late time $t\Omega_{ci} = 100$ when the turbulence is well-developed and a substantial gap exists between the upper and lower separatrix surfaces. The structure of the current in the interior is visualized with an isosurface of the current density. Notice that the main current sheet is in the center of the domain and is predominantly aligned in the y-direction. However, it is highly filamented and has formed oblique flux ropes as illustrated by the sample magnetic field lines (green). These flux rope structures form along the bottom (magnetosheath) separatrix in a manner similar to previously reported results for symmetric guide field regimes[20], where oblique flux ropes were observed along the high-density legs of the separatrices. However, for the present asymmetric layer there is a strong left/right asymmetry in the development of these flux ropes - i.e., the flux ropes are only observed along the right outflow. The reason appears to be straightforward. In symmetric guide field regimes, reconnection gives rise to high and low density separatrices, with the most intense current sheets forming along the high-density separatrices. Within asymmetric layers, this basic effect combines with the inherent density asymmetry across the sheet and selects one leg of the separatrix where the most intense current sheets form. Not surprisingly, this same result is also observed in 2D simulations (not shown), but the thin layers remain structurally stable since a resonance surface does not exist in 2D [20]. Within the outflow region, the plasma is quite turbulent with an assortment of electron inertial scale current structures.

The one-dimensional energy spectrum of the magnetic field is shown in Fig. 3 for the same time $t\Omega_{ci} \approx 100$ as Fig. 2. This spectrum was computed assuming that the mean field direction is determined by the uniform guide field. However, the local field direction is actually rotating by 90° across the reconnection layer. The red curve is the energy spectrum from a single time slice at $t\Omega_{ci} \approx 100.5$, while the blue curve was ob-

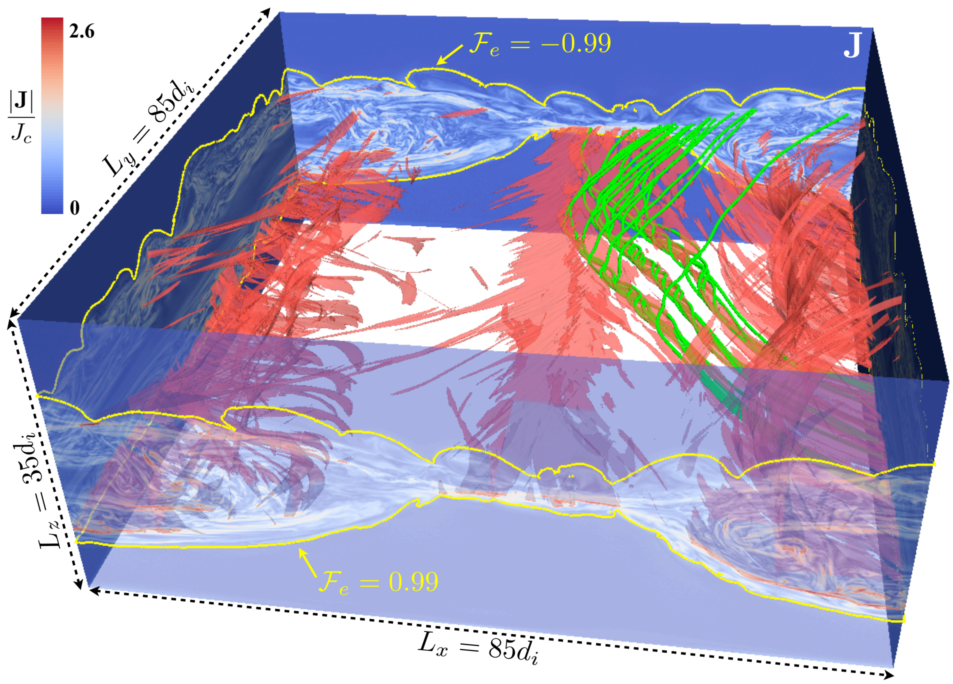

FIG. 2: Turbulent three-dimensional structure at time $t\Omega_{ci} \approx 100$ showing the current density around the perimeter of the simulation volume along with contours of the electron mixing fraction $\mathcal{F}_e$ as indicate (yellow lines). In the interior, an isosurface of current density (red) is shown along with a few sample magnetic field lines (green) to illustrate the formation of flux ropes.

tained by time averaging the magnetic field over the interval $t\Omega_{ci} \approx 99.7 \to 100.5$ using 40 equally spaced time slices. This time averaging tends to suppress the short-wavelength particle noise, but otherwise does not alter the rest of the spectrum. At longer wavelength, these results feature a clear power law with spectral index $k_\perp^{-2.7}$ in the range $k_\perp d_i \sim 1$ along with a gradual steepening for shorter wavelengths. While these 3D kinetic simulations are too small to permit an inertial range, the kinetic scale turbulence that is generated during reconnection compare favorably with spacecraft observation of reconnection jets in the Earth's magnetotail [44] as well as observation of turbulence in the solar wind [45, 46], and recent kinetic simulations of flow driven turbulence [47].

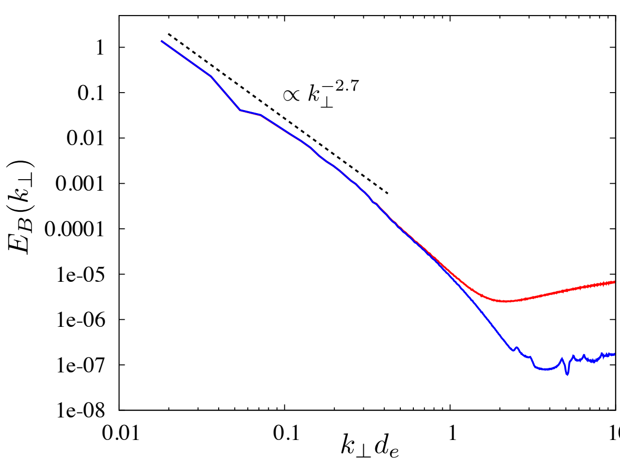

FIG. 3: Energy spectrum of the magnetic field corresponding to simulation shown in Fig. 2. The red curve is based on a single time slice at $t\Omega_{ci} \approx 100.5$, while the blue curve was obtained by averaging the magnetic field over the interval $t\Omega_{ci} \approx 99.7 \to 100.5$ using 40 equally spaced time slices.

For the purpose of this manuscript, we are primarily interested in measuring the influence of this turbulence on the *global* reconnection rate - i.e., the rate at which flux is transferred between the smooth upstream region in Fig. 1 into the mixed region. To proceed in this direction, it is important to characterize the structure of the magnetic field. In stochastic 3D magnetic fields, neighboring field lines undergo rapid spatial separation which can be characterized by the squashing factor [32–34], or the closely related Lyapunov exponent [14]. A flux tube with small but finite radius a_0 at $\ell = 0$ will map to an ellipse at $\ell = L_y$. To preserve the flux within the tube requires $\pi B_0(\ell) ab = \pi B_0(0) a_0^2$ where a and b are major and minor axes of the ellipse and $B_0(\ell)$ is the magnitude of the magnetic field along the central field line. Over longer distances the enclosed shape will become highly distorted as illustrated in the classic paper by Rechester and Rosenbluth [48]. Following the notation in Ref. [14], we can define the exponentiation factor σ for the mapping

$$\frac{a}{b} \equiv \mathrm{e}^{2\sigma(\ell)} \approx \left(\frac{a}{a_0}\right)^2 , \tag{2}$$

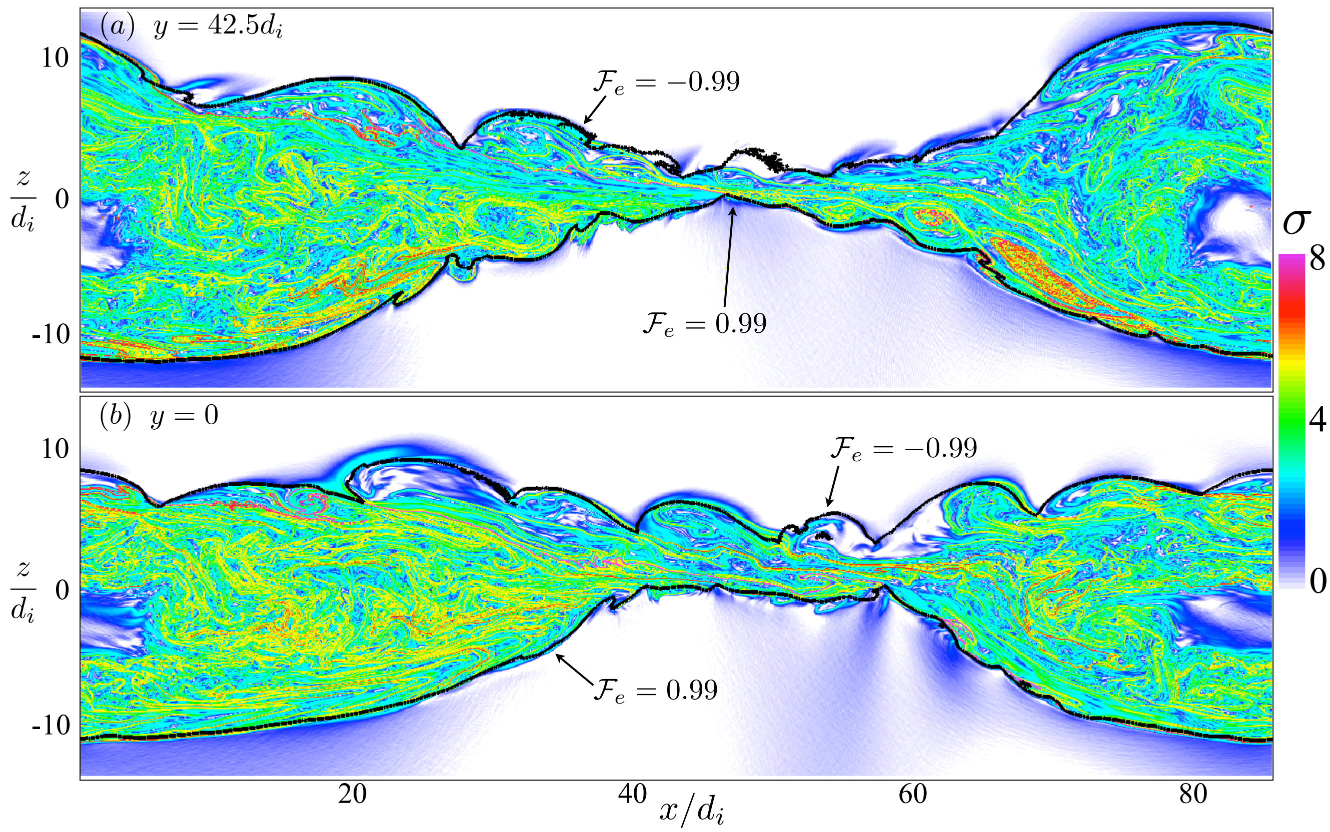

FIG. 4: Field line exponentiation factor σ as defined in Eq. (2) at time $t\Omega_{ci} = 100$ for the two x-z cross sections indicated: (a) $y = 42.5d_i$ and (b) $y = 0$. The integration length along each field line is $\ell = L_y = 85d_i$. The solid black lines correspond to contours of the electron mixing fraction $\mathcal{F}_e$ as indicated.

where the final equality assumes that $B_0(\ell)$ is weakly varying, which is true in the presence of an ambient guide field. In the limit $a \gg b$, the ratio a/b is equivalent to the squashing factor [32–34], while the quantity σ measures the maximum separation of neighboring field lines relative to an initial small separation a_0. To calculate σ from the simulation, we employ a spatial grid of seed points in the x-z plane and follow field line trajectories a distance L_y to compute the mapping between initial and final coordinates $\mathbf{x} \rightarrow \mathbf{X}$. The Jacobian for this map $\mathcal{J} = \partial\mathbf{X}/\partial\mathbf{x}$ is used to form the symmetric displacement tensor $\mathcal{D} \equiv \mathcal{J}\mathcal{J}^T$ and the field line exponentiation factor is given by

$$\sigma = \ln(\rho_{max}^{1/2}) \; , \tag{3}$$

where ρ_{max} is the maximum eigenvalue of $\mathcal{D}$.

The resulting values of σ for this simulation are shown in Fig. 4 at time $t\Omega_{ci} = 100$ for two x-z cutting planes through the 3D volume in Fig. 2. The top panel corresponds to a slice through the center of the domain, while the bottom panel is along the edge. In each case, the solid black lines correspond to contours of the electron mixing fraction $\mathcal{F}_e$ as indicated. Notice that σ is quite small above the $\mathcal{F}_e = -0.99$ contour and below the $\mathcal{F}_e = 0.99$ contour, indicating that neighboring magnetic field lines remain close when mapped across the system. However, there is a rapid increase in σ across these boundaries and the interior region of mixed plasma is clearly associated with a chaotic 3D magnetic field, with peak values of the exponentiation factor approaching $\sigma \approx 8$. The boundary of increasing σ is for the most part well-correlated with the contours of the mixing fraction $\mathcal{F}_e$, suggesting these may indeed correspond to topological boundaries. In order to further verify this idea, we traced field lines through the system ten times for seed points above and below these apparent topological boundaries. For seed points in the small σ regions, the field lines stay on the same side of the layer and are well-organized into apparent flux surfaces, while for seed points in the large σ region the field lines quickly spread throughout the mixed volume (see animation in Ref. [49]).

These results imply that the magnetic field is comprised of three topological regions. In the top and bottom regions, the magnetic field lines remain on the same side of the layer and the flux surfaces are well-defined. In the central region, the magnetic field lines are stochastically mixed across both sides of the layer. The mixing fraction of electrons then closely mirrors these topologies and can be used to rapidly infer the separatrix surfaces between the mixed and unmixed regions. In the magne-

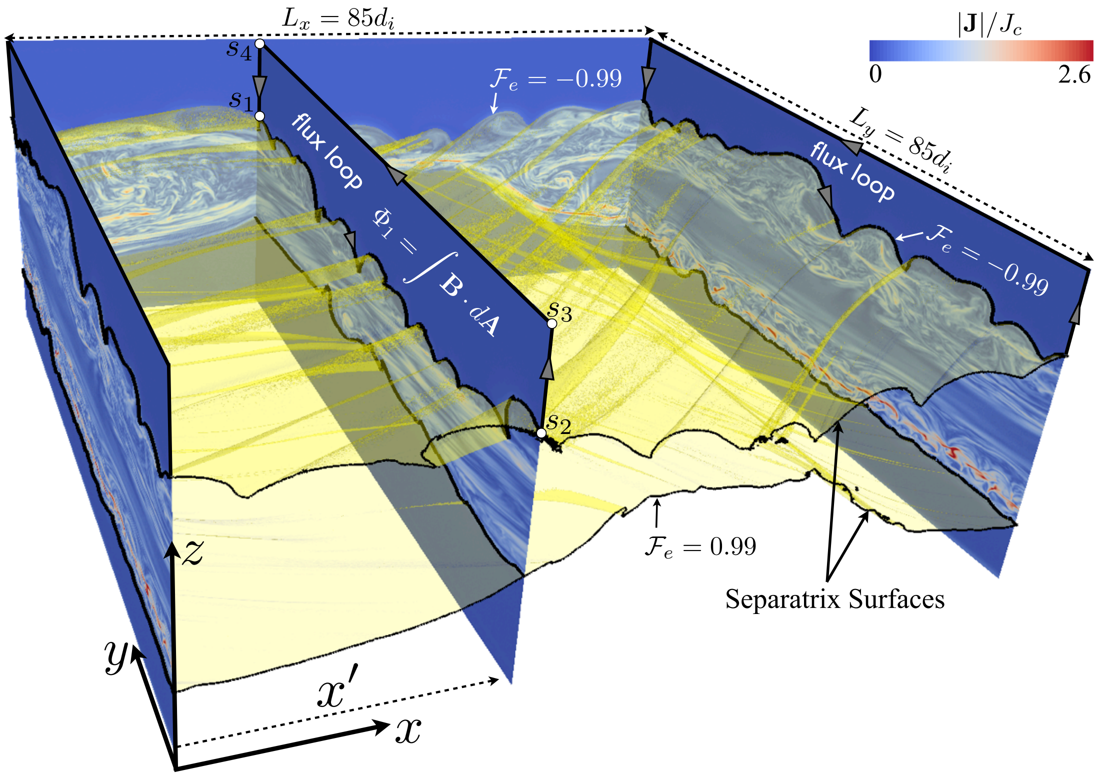

FIG. 5: Three-dimensional structure of the separatrix surfaces (translucent yellow) identified by isosurfaces of electron mixing fraction $\mathcal{F}_e = 0.99$ and $\mathcal{F}_e = -0.99$. The blue cutting planes show the current density normalized by J_c. Two example flux loops are shown for the top region at $x = x'$ and $x = L_x$.

tosphere, there may be other observational signatures of these separatrix surfaces, such as the sudden drop-out of the high-energy magnetospheric electrons often observed across the magnetopause.

Given these topological regions identified in Fig. 4, it is now straightforward to evaluate the global reconnection rate by tracking the time evolution of magnetic flux within the top and bottom regions, which contain the flux responsible for driving reconnection. The basic idea is illustrated in Fig. 5 which shows the 3D structure of the separatrix surfaces using translucent isosurfaces of the electron mixing fraction. Two example flux loops are shown for the top region at $x = x'$ and $x = L_x$. The magnetic flux through an arbitrary loop at x' is given by

$$\Phi_1(x') \equiv \int \mathbf{B} \cdot d\mathbf{A} \ ,$$

and likewise for the flux $\Phi_0(x')$ through the equivalent loop on the bottom side (not shown). If these surfaces identified by the electron mixing fraction correspond to the true separatrix surfaces, then the fluxes $\Phi_1(x')$ and $\Phi_0(x')$ will not depend on the choice of x' and the reconnection rate will not depend on which loop we consider. Thus evaluating the fluxes for the entire range of $x' = 0 \rightarrow L_x$ will give an error estimate for the rate.

To relate this approach back to the electric field, consider Faraday's law applied to one of these loops

$$\frac{d\Phi}{dt} = -c \oint \mathbf{E} \cdot d\mathbf{s} = -c \int_{s_2}^{s_1} \mathbf{E} \cdot d\mathbf{s} \ , \tag{4}$$

as indicated in Fig. 5. Note that along z-boundary ($s_3 \rightarrow s_4$) the transverse electric field vanishes due to the conducting boundary conditions, while the contribution from $s_2 \rightarrow s_3$ cancels the contribution from $s_4 \rightarrow s_1$ due to the periodic boundary condition in the y-direction. Thus the time changing flux through the loop is equal to the line integral of the electric field along the separatrix surface. In general this path does not correspond to a field line, except at early times in the simulation when the two separatrix surfaces very nearly intersect along what appears to be a separator (i.e., the magnetic field line common to both surfaces). During this phase, the reconnection rate must be the same for the top and bottom regions $\dot{\Phi}_1 = \dot{\Phi}_0$ and is equal to the line integral of the parallel electric field along the separator. However, at later times when a turbulent gap opens between the two separatrix surfaces, it is no longer possible to offer this simple interpretation and furthermore there is no reason why the reconnection rates must be the same in the top and bottom regions.

In order to facilitate direction comparison with the equivalent 2D simulation, we define the normalized reconnection rate based on the flux per unit length in the

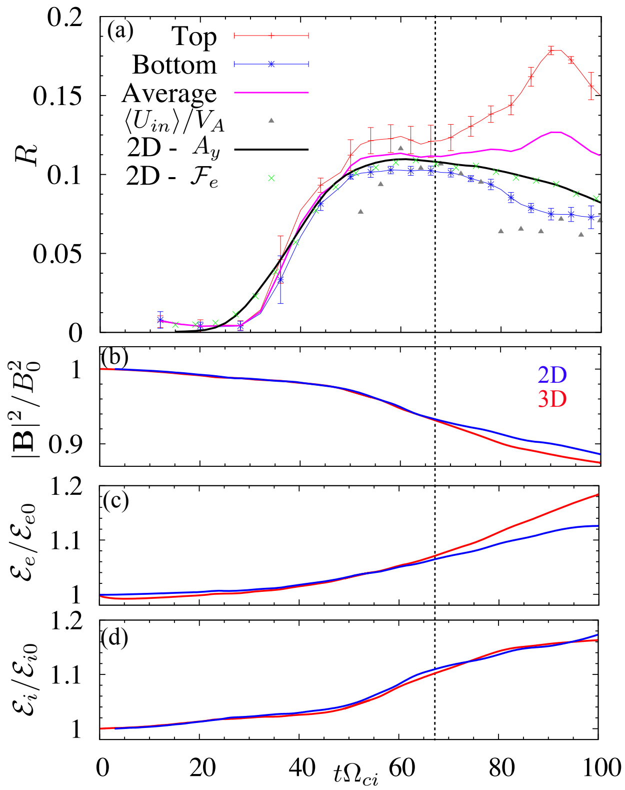

FIG. 6: Rate computed from Eq. (5) based on the top (red), bottom (blue) and average (purple) fluxes and using $|\mathcal{F}_e| = 0.99$ to fined the separatrix surfaces. Grey triangles are the inflow rates in Eq. (6) applied to the bottom region. The black curve is the 2D reconnection rate measured from the flux function A_y, while the green crosses are the 2D rate obtained from the mixing approach with $|\mathcal{F}_e| = 0.99$. Bottom panels show time evolution of the (b) magnetic field energy, (c) electron and (d) ion kinetic energies for the 3D (red) and 2D (blue) simulations. In the magnetic field energy, the portion associated with the external guide field has been removed, and the kinetic energies are normalized to their initial value. The total energy for both cases increased by 3% due to numerical heating in the electrons. This numerical heating was subtracted from results shown in panel (c).

y-direction

$$R = \frac{1}{B_0 V_A L_y}\frac{d\Phi}{dt}\ , \tag{5}$$

where $V_A = B_0/(4\pi n_0 m_i)^{1/2}$ is the Alfvén velocity based on the initial magnetic field and density on the bottom side of the layer. To estimate the errors arising from using $\mathcal{F}_e$ to identify the separatrix surfaces, the reconnection rate obtained from Eq. (5) is evaluated for 73 equally spaced flux loops between $x' = 0 \rightarrow L_x$ on both the top and bottom. The simulation time slices were separated by $\Delta t\Omega_{ci} = 4$ and second order central differencing was used to evaluate $\dot{\Phi}$. In order to identify the separatrix surfaces, we typically employ a mixing fraction of $|\mathcal{F}_e| = 0.99$. However, as shown in Appendix A, the reconnection rate is not very sensitive to this choice over the range $\mathcal{F}_e = 0.90 \rightarrow 0.995$.

The resulting reconnection rate for this simulation is shown in Fig. 6a for the top (red) and bottom (blue) regions. The solid line is the average value from the 73 flux loops, while the error bars correspond to the standard deviation. The estimated uncertainty from this approach is typically 5-10%, which should be sufficiently accurate for most purposes. The average between the top and bottom rates is shown in purple while the black line is the reconnection rate obtained from a corresponding 2D simulation with the same physics parameters. For this 2D simulation, the reconnection rate was computed directly using the flux function in the same manner as typically done in periodic simulations [50]. As a consistency check, we also computed the reconnection rate for this 2D case using Eq. (5) with mixing fraction $|\mathcal{F}_e| = 0.99$ to determine the separatrices. Notice that the results (green crosses) are in nearly perfect agreement with the rate obtained from the flux function, confirming the validity of this approach. In this 2D run, the separatrices on the two sides of the layer always intersect at the x-line, and as a result the rate obtained from the mixing fraction remains the same on both sides.

To elucidate the relationship between Eq. (5) and commonly employed inflow estimates of the reconnection rate, consider a flux loop in Fig. 5 located at $x' = L_x/2$ near the dominant inflow. If the separatrix surface along this loop is not highly structured, we can close the loop by drawing a straight line from $s_1 \rightarrow s_2$. When this approximate path is not too different then actual path, we can combine Eqns. (4)-(5) to obtain

$$R \approx \frac{c\langle E_y\rangle}{B_0 V_A} \equiv \frac{\langle U_{in}\rangle}{V_A}\ , \tag{6}$$

where $\langle\,\rangle$ is the average along the straight line $(s_1 \rightarrow s_2)$ and $U_{in} \approx cE_y/B_0$ is the approximate inflow velocity assuming that the upstream magnetic field B_x remains close to the initial asymptotic value B_0. The grey triangles in Fig. 6b correspond to Eq. (6) for the bottom region, where a coherent inflow is observed throughout the evolution (see Fig. 1). Not surprisingly, the estimate in Eq. (6) is roughly correct, and the physical connection back to plasma inflow is clear. However, note that Eq. (6) is highly inaccurate on the top boundary (not shown) for times $t\Omega_{ci} > 60$ as the separatrix surface becomes corrugated, and many smaller inflow and outflow regions develop.

These 3D reconnection rates (both top and bottom) are in very good agreement with the 2D result up until $t\Omega_{ci} \approx 60$. At later times, the rate in the top region is significantly enhanced while the rate in the bottom region continues to track the 2D result. One obvious question is whether this enhanced 3D reconnection rate modifies either the energy conversion timescale or the partitioning of energy between electron and ions. Surprisingly, these changes are far more subtle. The rate of decrease in the magnetic field energy (see Fig. 6b) becomes slightly faster at the same time $t\Omega_{ci} \approx 65$ that the reconnection rate is enhanced. This small additional heating goes to the electron kinetic energy $\mathcal{E}_e$ as shown in Fig. 6c, while the ion kinetic energy $\mathcal{E}_i$ evolution is nearly identical to the 2D case as shown in Fig. 6c.

The physics responsible for this enhanced rate in the top region is not yet well-understood. However, the enhancement is clearly correlated with the development of vortex tubes along this boundary, which appear to be driven by the recirculation of the reconnection outflow jets. At the magnetopause, this type of interaction between reconnection outflows may occur commonly due to the presence of multiple active x-lines, as reported in recent observations [51]. Within 2D models, it is energetically more difficult for the reconnection outflows to generate vortices, since it is necessary to wrap-up the in-plane component of the magnetic field (i.e., which is stabilizing to Kelvin-Helmholtz type instabilities). However, in 3D the wavevector for the perturbation can rotate to an oblique angle in order to minimize the energy penalty associate with generating a vortex tube. These oblique vortex tubes along the top boundary cause the separatrix surface to become highly corrugated with many cusp like regions (see Fig. 4) associated with the rollup, which may in turn cause local shearing of the magnetic field and small-scale reconnection in each cusp. In addition, a turbulent mixed region (or gap) is observed to form along the entire spatial extent in the x and y-directions, so that the separatrix surfaces no longer intersect.

These results suggest that mixing of field lines across the layer is more easily modified by the 3D dynamics than the physics responsible for the energy conversion. In the following section, we will consider this issue further for a case where the turbulence is driven even more strongly by a pre-existing flow.

III. VORTEX-INDUCED RECONNECTION

Along the lower-latitude flank regions of the magnetopause boundary, there is strong velocity shear which can drive the Kelvin-Helmholtz (KH) instability as shown by spacecraft observations [52, 53]. Two-dimensional simulations have demonstrated that KH can compress the magnetopause current layer and drive reconnection in regions where it would not normally occur [54–57]. This *vortex-induced* reconnection has important implications for mixing across the magnetopause. Recently, the first 3D fully kinetic simulations of this process have demonstrated the formation of small-scale flux ropes around the perimeter of the vortices, leading to a complicated evolution in which reconnection and the flow turbulence are coupled [25]. In contrast to the example in Sec. II, computing the reconnection rate in these regimes is much more difficult even with 2D models due to the large number of interacting magnetic islands within the flow vortices. As a result, there is not a single large-scale coherent inflow and outflow, but rather many smaller scale reconnection sites which vary rapidly in space and time. Thus estimating the reconnection rate based on the inflow is not workable. For clarity, we first give a brief description of the setup and refer interested readers to Ref. [25] for further details of this simulation and comparisons with spacecraft observations.

A. Simulation Setup

The initial condition is a modified Harris-type layer with magnetic field $\mathbf{B}(z) = B_0 \tanh(z/\lambda)\mathbf{x} + B_y\mathbf{y}$ where $\lambda = 2d_i$ is the half-thickness of the layer and $B_y = 5B_0$ is a uniform guide field. The plasma is composed of two components with total density $n(z) = n_h \text{sech}^2(z/\lambda) + n_0$ where n_0 is the uniform background density and $n_h = 0.08n_0$ is the central density for the Harris-type component which supports the current $J_y = J_c\ \text{sech}^2(z/\lambda)$ where $J_c = cB_0/(4\pi\lambda)$. To form the velocity shear layer, particles are initialized with a drifting Maxwellian distributions with bulk velocity $V_x = V_0 \tanh(z/\lambda)$. The temperature is uniform with $T_i/T_e = 3$ and the mass ratio is $m_i/m_e = 25$. We normalize all quantities using the background density n_0 and the reconnecting component of the magnetic field B_0. With this choice, the other simulation parameters are $\omega_{pe}/\Omega_{ce} = 8$, $v_{the}/c = 0.15$, $V_0 = 7V_A$ and $\beta_{x0} = 8\pi n_0(T_i + T_e)/B_0^2 = 12.5$. The system size is $L_x \times L_y \times L_z = 60d_i \times 30d_i \times 40d_i$ with $2048 \times 1024 \times 1368$ cells and a total of 0.7×10^{12} computational particles. As described in Ref. [25], the size of the simulation was chosen to allow two wavelengths of the most unstable KH mode. The boundary conditions are periodic in the x and y-directions, while on the z-boundaries particles are reflected and the field boundary conditions are conducting. A small perturbation is added to the velocity to initiate the development of the KH instability as described in Ref. [25]

B. Results

The overall time evolution for this simulation is illustrated in Fig. 7 for x-z planes located at $y = 0$ in the 3D volume. The left panels show the time evolution of the exponentiation factor σ computed by integrating for a distance $\ell = L_y = 30d_i$ along each field line, while right panels show the evolution of the current density. In both cases, the black lines show the contours of electron mixing fraction $\mathcal{F}_e = 0.99$ and $\mathcal{F}_e = -0.99$ as indicated. As shown in Figs. 7a-b, the initial nonlinear evolution of the two KH vortices leads to the stretching of the in-plane field and the generation of intense current layers, which are unstable to a spectrum of tearing instabilities [25]. As reconnection develops in these thin layers, the mixed region rapidly expands and becomes turbulent. This flow driven turbulence continues to generate new thin current layers throughout the mixed volume (determined by $\mathcal{F}_e$), which gradually expands outward in the z-direction. In

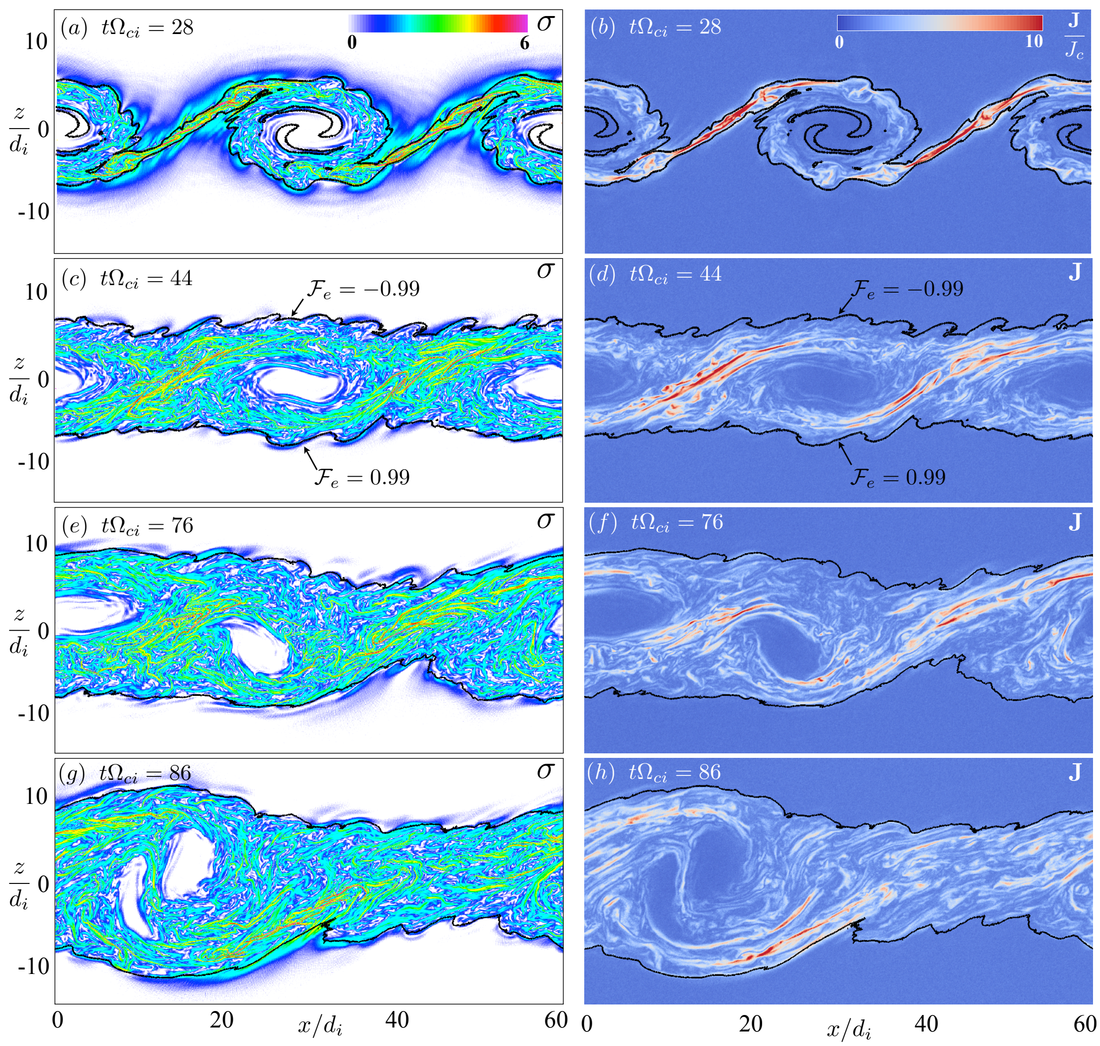

FIG. 7: Time evolution of vortex-induced reconnection showing the field line exponentiation factor σ (left panels) and the magnitude of the current density (right panels) normalized to the initial value $J_c = cB_0/(4\pi\lambda)$ for x-z slices at $y = 0$. The integration length along each field line is $\ell = L_y = 30d_i$. The black lines correspond to contours of the electron mixing fraction $\mathcal{F}_e = 0.99$ and $\mathcal{F}_e = -0.99$ as indicated.

the final stage, the two primary vortices undergo merging as the volume of mixed field lines (and plasma) continually increases [see panels (g)-(h)]. Throughout this evolution, the structure of the magnetic field as characterized by σ is chaotic within the mixed volume, with the exception of the interior region of the vortices, where the flow shear is weak and the resulting field structure remains simple. Notice that the regions with largest σ are well correlated with the most intense current sheets. However, while the spatial thickness of the current sheets range from d_i down to a few d_e, the thin ribbons of strong σ are much thinner, since σ is not limited by any kinetic scale. The volume of chaotic magnetic field measured by σ remains generally well-correlated with the volume of mixed plasma determined by the mixing fraction $\mathcal{F}_e$. This correlation supports our interpretation of these boundaries as separatrix surfaces.

To further test this idea, field lines were traced through system 32 times to create a rough Poincaré map as shown in Fig. 8. The green field lines correspond to a small group of seed points placed near $x = L_x/2$ above the $\mathcal{F}_e$ contour. Notice these green lines remain in this upper region and are well-organized into apparent flux surfaces. In contrast, two small groups of seed points were placed inside the mixed region near the vortex edge (black) and near the flow stagnation region (yellow). Within a few passes through the system, these field lines are connected to large regions of the mixed volume. Furthermore, while these field lines approach the threshold contours of the electron mixing fraction $\mathcal{F}_e = 0.99$ and $\mathcal{F}_e = -0.99$ as indicated, they do not cross into the upper and lower regions. This is a clear demonstration that these boundaries identified by the mixing fraction indeed correspond to topological boundaries of the magnetic field (i.e., separatrix surfaces), and that mixing of magnetic field lines across the layer proceeds in tandem with the mixing of

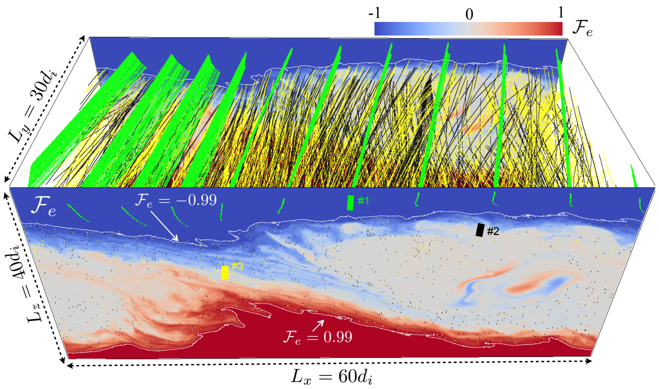

FIG. 8: Structure of the 3D magnetic field lines for the simulation of vortex-induced reconnection at time $t\Omega_{ci} = 96$. The front and back surfaces show the electron mixing fraction $\mathcal{F}_e$. As indicated in the figure, three small groups of initial seed points are used to trace the magnetic field through the system 32 times: (1) green corresponds to the region above the $\mathcal{F}_e = -0.99$ boundary, (2) black corresponds to seed points at the edge of the vortex, and (3) yellow corresponds to seed points near the stagnation region between vortices.

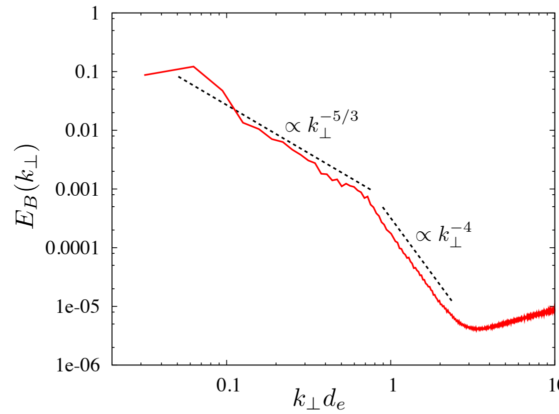

FIG. 9: Energy spectrum of the magnetic field fluctuations at time $t\Omega_{ci} = 105$ for the simulation of vortex-induced reconnection.

particles.

The one-dimensional energy spectrum of the magnetic field is shown in Fig. 9 at time $t\Omega_{ci} = 105$ after the merging has occurred between the two initial vortices. This spectrum was computed in the same manner as Fig. 3 by assuming that the mean field direction is determined by the guide field. This approximation is better justified for this simulation since the guide field is initially 5× stronger then the reconnecting field. However, as the simulation proceeds the in-plane field is amplified by the flow and at the time shown in Fig. 9 the guide field is only $\sim 2\times$ stronger then the peak in-plane fields. The spectrum shown in Fig. 9 features a power-law for longer wavelengths with spectral index $\sim k_\perp^{-5/3}$, followed by a pronounced steepening for shorter wavelengths $k_\perp d_e \gtrsim 1$.

The time evolution of the reconnection rate was computed by evaluating Eq. (5) for 64 equally spaced flux loops between $x' = 0 \rightarrow L_x$ on both the top and bottom, in the same manner as illustrated conceptually in Fig. 5. The average reconnection rate is shown in Fig. 10a for the top (red) and bottom (blue) regions, while the error bars correspond to the standard deviation, and the green curve corresponds to the average between the two regions. To compute the time derivative of the flux $\dot{\Phi}$, time slices separated by $\Delta t\Omega_{ci} = 4$ were used with second order central differencing. For comparison, the reconnection rate in the corresponding 2D simulation (black) is also computed using the mixing approach, since tracking the flux function is prohibitively difficult for these regimes. In both cases, the first burst of reconnection associated with the formation of the initial vortices occurs between $t\Omega_{ci} = 20 \rightarrow 40$ with the peak 3D rate $R \approx 0.32$ nearly 20% larger than in 2D. During the interval $t\Omega_{ci} = 40 \rightarrow 75$, the 2D rate $R \approx 0.02$ remains much smaller than the 3D rate $R \approx 0.06$.

Notice that the 3D rates on the top and bottom are equal within the error bars up through $t\Omega_{ci} \approx 75$ where the vortex merging is starting (see Fig. 7ef). During the coalescence of these vortices, a new thin current sheet is formed in the 2D simulation (see Ref. [25]) which produces a strong burst of reconnection at time $t\Omega_{ci} \approx 90$ in Fig. 10a. In contrast, the 3D simulation features a broader turbulent layer at late time. As a result, the second burst in reconnection is much weaker along the bottom boundary and is not apparent at all along the top boundary. To estimate the sensitivity of the average 3D rate to the threshold on $\mathcal{F}_e$, the electron mixing fraction was varied over the range $\mathcal{F}_e = 0.90 \rightarrow 0.995$ as shown in Appendix A. As before, the reconnection rate is insensitive to the specific choice of $\mathcal{F}_e$.

While the error bars in these 3D reconnection rates are somewhat larger in Fig. 10a than in the previous example, they are still sufficiently small to illustrate some important qualitative and quantitative differences. In particular, the initial burst of reconnection is clearly more effective in 3D and this is followed by a turbulent evolution in which the rate proceeds significantly faster than in 2D. As a result, the late time burst of reconnection is far less than in the 2D simulation.

Assuming these trends hold for larger systems, the 3D evolution may proceed by a continual turbulent mixing, while the 2D evolution will remain bursty. Note that within the 2D simulation, localized reconnection can proceed within a current sheet only when the in-plane field across the sheet reverses sign. Thus many thin sheets will remain stable to reconnection within 2D. In contrast, in 3D tearing perturbations can rotate to an oblique angle [20, 25] and it is easier for reconnection to proceed in nearly any extended layer. As a consequence, it is harder for the 3D simulations to maintain stressed regions in the same manner as in 2D. This physics is apparent in Fig. 10b, which compares the time evolution of the magnetic energy between 2D and 3D. Consistent with the

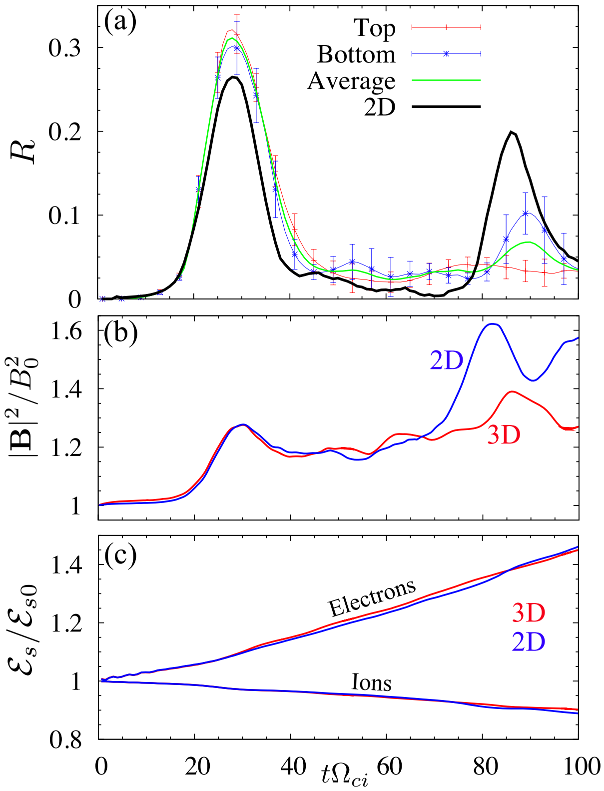

FIG. 10: (a) Reconnection rate computed from Eq. (5) based on the time changing flux in the top $\dot{\Phi}_1$ and bottom $\dot{\Phi}_1$ regions and assuming $|\mathcal{F}_e| = 0.99$ to determine the separatrix surfaces. The green curve is from the average $(\dot{\Phi}_0 + \dot{\Phi}_1)/2$ while the black curve is the reconnection rate from the corresponding 2D simulation measured directly using the mixing approach with $|\mathcal{F}_e| = 0.99$. Bottom panels show time evolution of the (b) magnetic field energy and (c) electron and ion kinetic energies for the 3D (red) and 2D (blue) simulations. In the magnetic field energy, the portion associated with the external guide field has been removed, and the kinetic energies are normalized to their initial value.

above argument, more magnetic energy is accumulated in the 2D case at late time $t\Omega_{ci} > 70$, as the flow drives additional wrapping of the in-plane field associated with vortex merging.

In contrast to example in Sec. II which was driven by the magnetic shear, this simulation is really driven by the ion flow which continually pumps energy back into the magnetic field. Through the simulation the energy in the flow is much larger than the magnetic field (excluding the external guide field). Thus while the small differences in the magnetic field evolution in Fig. 10b are interesting, this does not significantly alter the evolution of either the electron or ion energy, as shown in Fig. 10c. Together with the previous example in Sec. II, these results imply that the 3D turbulence can influence the mixing of magnetic field lines and particles across the layer, but does not substantially alter the energy conversion time scales.

IV. SUMMARY

The influence of three-dimensional dynamics and turbulence remains one of the most challenging problems in reconnection physics. Recent advances in computing are permitting 3D kinetic simulations in which turbulence is generated spontaneously within initially laminar current layers. For the examples shown here relevant to the magnetopause, the turbulence is driven by the combined influence of magnetic and/or velocity shear, and is dominated by coherent structures including flux ropes, current sheets and flow vortices. The resulting magnetic field quickly becomes chaotic within the reconnection layer and outflow regions, and thus integrating the parallel electric field to compute the reconnection rate [37, 38] is challenging.

In this paper, we propose an alternative approach for computing the reconnection rate, which relies upon the mixing of electrons to rapidly identify the magnetic topology of the layer. The basic idea is simple and physically well-motivated. Particles originating from separate side of the layer are tagged, so that we can compute the subsequent evolution of the mixing fraction. We have shown that a simple threshold on the electron mixing fraction $\mathcal{F}_e$ can be used to approximately identify the *separatrix surfaces* - corresponding to the surface of field lines that encompass flux from a single source. These separatrix surfaces divide the field lines into three topologies: (1) an upper region with smooth magnetic field, (2) a corresponding lower region with smooth field and (3) a turbulent region in which both the field lines and particles are mixed. Within this mixed region, the magnetic field is chaotic as shown by the field line exponentiation factor σ. The separatrix surfaces inferred by a threshold on the mixing fraction $\mathcal{F}_e$ are well-correlated with regions where σ becomes large. As a final check, we have verified these topologies directly by integrating magnetic field lines many times through the system to create an approximate Poincaré map. However, we note this can only be done for simulations with periodic boundary conditions, while the idea of using mixing to identify separatrix surfaces is more general and could in the future be applied to open systems as well.

While integrating the magnetic field lines to determine topology is very expensive, the approximate approach based on mixing is obtained automatically as part of the kinetic simulation. This permits the time evolution of the magnetic flux to be tracked separately within the upper and lower regions, which contain the flux driving the reconnection. The uncertainties in this approach due to the differences between the exact separatrix surfaces (determined by field topology) and the approximate surfaces (inferred by $\mathcal{F}_e$) can be estimated by tracking the flux for a range of loops as illustrated in Fig. 5. For the asymmetric layer shown in Sec. II, the error bars are typically 5-10% while for the vortex-induced reconnection setup shown in Sec. III the errors are somewhat larger.

The key physical assumption implicit in this approach is that mixing proceeds primarily through the parallel streaming of particles along newly reconnected field lines. Due to their small gyroradius and rapid thermal motion, electrons give a better approximation than ions. However, we have verified that the ion mixing fraction gives very similar rates, but with larger error bars corresponding to bigger uncertainties in the location of the separatrix surfaces. For the two examples shown here, the plasma is laminar in the upstream regions and magnetic field is well-organized into flux surfaces. It is not clear that the present method would work in the presence of a strong pre-existing turbulence in the upstream region, since it may no longer be possible to define separate magnetic topologies (i.e., the field lines may be chaotically mixed in the entire domain). Another limit in which the method will likely break down is due to the presence of strong electrostatic turbulence that causes particle mixing to occur separately from field line mixing. In this limit, one could still track the evolution of the flux, but the separatrix surfaces would need to be determined by field line integration rather than through the particle mixing.

The two examples simulations used to illustrate this approach feature a number of interesting differences in the reconnection rate associated with the development of kinetic turbulence. For the asymmetric layer shown in Sec. II, the 3D reconnection rate is in good agreement with the corresponding 2D simulation up until the point when reconnection outflow begins to drive vortex tubes along the upper separatrix surface. As shown in Fig. 6, this leads to a $\sim 70\%$ enhancement of the reconnection rate associated with this upper region. In a similar manner, the case of vortex-induced reconnection in Sec. III is dominated by strong Alfvénic shear flow throughout the evolution, leading to significant differences as illustrated in Fig. 10. After the initial strong burst of reconnection, the development of 3D turbulence largely suppresses the bursty behavior observed in 2D simulations, and gives rise to a continual mixing of particles and field lines across the layer. Thus it appears the 3D evolution is qualitatively different than observed in 2D.

Despite these differences in the reconnection rate, the time evolution of the energy conversion rates are remarkably similar to the corresponding 2D simulation for both of the examples shown in this paper. This clearly illustrates that there is not a one-to-one relationship between the reconnection rate and the energy conversion rate. This is true even within 2D, but is particularly apparent in these 3D simulations. If magnetic reconnection is defined based on the mixing of flux between distinct magnetic topologies, it is possible for enhanced mixing of the field lines to occur without enhanced energy conversion. While many applications of reconnection involve a bursty release of energy (solar flares, magnetospheric substorms, sawtooth oscillations, etc.) in some applications the mixing of plasma from different sources is equally important, as for example, the entry of solar wind plasma into the magnetosphere. While this initial study only considered two cases, the results suggest that 3D dynamics and turbulence can enhance the mixing of field lines (and particles) between topologies, but that modifying the basic energy conversion time scale is much harder in these kinetic regimes.

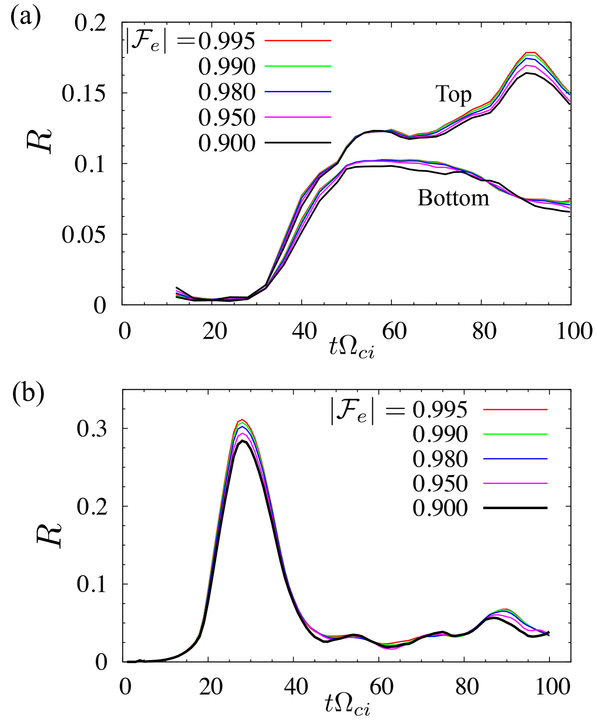

FIG. 11: Sensitivity of the 3D reconnection rate to specified threshold on the electron mixing fraction $|\mathcal{F}_e| = 0.90 \rightarrow 0.995$ for (a) the top and bottom regions of the asymmetric layer shown in Sec. II and (b) the average value for the vortex-induced example in Sec. III.

Appendix A: Sensitivity to Mix Fraction

In order to estimate the sensitivity of this approach, the threshold on the electron mixing fraction was varied over the range $\mathcal{F}_e = 0.90 \rightarrow 0.995$ as shown in Fig. 11a for the asymmetric reconnection layer in Sec. II and in Fig. 11b for the vortex-induced example shown in Sec. III. In both cases, these results demonstrate that the gradient in the mixing fraction is very steep near these boundaries, and thus the reconnection rate is insensitive to the specific choice. Since these simulations typically employ $N_p \sim 100$ particles per cell, a physically reasonable threshold should be in the range $|\mathcal{F}_e| \approx 1 - 1/N_p$

Acknowledgments

We are grateful for support from NASA (NNX12AD30G, Heliophysics Theory and Geospace Science), from NSF (0904734, 1104815), and DOE

(DE-SC0004662). This research used resources of the Oak Ridge Leadership Computing Facility at the Oak Ridge National Laboratory, which is supported by the Office of Science of the U.S. Department of Energy under Contract No. DE-AC05-00OR22725. Additional simulations and analysis was performed with Los Alamos institutional computing. We would like to acknowledge useful discussions with J.D. Scudder, V.S. Titov, A. Boozer and J. Dorelli.

---

[1] H. Ji and W. Daughton, Phys. Plasmas **18** (2011).
[2] H. Karimabadi and A. Lazarian, Phys. Plamas **20**, 112102 (2013).
[3] H. Karimabadi, V. Roytershteyn, W. Daughton, and Y.-H. Liu, Space Sci. Rev. **178**, 307323 (2013).
[4] D. Pontin, Advances in Space Research **47**, 1508 (2011).
[5] W. Matthaeus and S. Lamkin, Phys. Fluids **29**, 2513 (1986).
[6] A. Lazarian and E. Vishniac, ApJ **517**, 700 (1999).
[7] G. Kowal, A. Lazarian, E. T. Vishniac, and K. Otmianowska-Mazur, ApJ **700**, 63 (2009).
[8] W. Matthaeus and M. Velli, Space Science Reviews **160**, 145 (2011), ISSN 0038-6308, URL `http://dx.doi.org/10.1007/s11214-011-9793-9`.
[9] Z. B. Guo, P. H. Diamond, and X. G. Wang, Astrophys. J. **757**, 173 (2012).
[10] G. Eyink, E. Vishniac, C. Lalescu, A. Hussein, K. Kanov, K. Buerger, R. Burns, C. Meneveau, and A. Szalay, Nature **497**, 466 (2013).
[11] H. Higashimori, N. Yokoi, and M. Hoshino, Phys. Rev. Lett. **110**, 255001 (2013).
[12] P. P.J. Morrison, Phys. Plasmas **7**, 2279 (2000).
[13] A. R. Yeates and G. Hornig, Phys. Plasmas **18**, 102118 (2011).
[14] A. H. Boozer, Phys. Plasmas **19**, 112901 (2012).
[15] A. H. Boozer, Phys. Plasmas **19**, 092902 (2012).
[16] K. Bowers, B. Albright, L. Yin, W. Daughton, V. Roytershteyn, B. Bergen, and T. Kwan, Journal of Physics: Conference Series **180**, 012055 (2009).
[17] G. Paschmann, M. Øieroset, and T. Phan, Space Science Reviews **178**, 385 (2013).
[18] T. Moore, J. Burch, W. Daughton, S. Fuselier, H. Hasegawa, S. Petrinec, and Z. Pu, Journal of Atmospheric and Solar-Terrestrial Physics **99**, 32 (2013).
[19] A. Galeev, M. Kuznetsova, and L. Zelenyi, Space Sci. Rev. **44**, 1 (1986).
[20] W. Daughton, V. Roytershteyn, H. Karimabadi, L. Yin, B. J. Albright, B. Bergen, and K. J. Bowers, Nature Physics **7**, 539 (2011).
[21] Yi-Hsin Liu, W. Daughton, H. Karimabadi, H. Li, and V. Roytershteyn, Phys. Rev. Lett. **110**, 265004 (2013).
[22] E. Leonardis, S. C. Chapman, W. Daughton, V. Royterhsteyn, and H. Karimabadi, Phys. Rev. Lett. **110**, 205002 (2013).
[23] R. Wang, R. Nakamura, Q. Lu, and et. al., J. Geophys. Res. **117**, A07223 (2012).
[24] S. Y. Huang, M. Zhou, F. Sahraoui, A. Vaivads, X. H. Deng, M. Andr, J. S. He, H. S. Fu, H. M. Li, Z. G. Yuan, et al., Geophys. Res. Lett. **39**, L11104 (2012).
[25] T. K. M. Nakamura, W. Daughton, H. Karimabadi, and S. Eriksson, J. Geophys. Res. **118**, 5742 (2013).
[26] L. Yin, W. Daughton, H. Karimabadi, B. Albright, K. J. Bowers, and J. Margulies, Phys. Rev. Lett. **101**, 125001 (2008).
[27] J. Dorelli and A. Bhattacharjee, J. Geophys. Res. **114**, A06213 (2009).
[28] A. L. Haynes and C. E. Parnell, Phys. Plasmas **17**, 092903 (2010).
[29] C. Komar, P. A. Cassak, J. C. Dorelli, A. Glocer, and M. M. Kuznetsova, J. Geophys. Res. **118**, 49985007 (2013).
[30] G. Siscoe, G. M. Erickson, B. U. . Sonnerup, N. C. Maynard, K. D. Siebert, D. R. Weimer, and W. W. White, J. Geophys. Res. **106**, 13015 (2001).
[31] K. Schindler, M. Hesse, and J. Birn, J. Geophys. Res. **93**, 5547 (1988).
[32] E. R. E.R. Priest and P. Dmoulin, J. Geophys. Res. **100**, 23443 (1995).
[33] V. Titov, G. Hornig, and P. Dmoulin, J. Geophys. Res. **107**, 1164 (2002).
[34] A. S. Richardson and J. M. Finn, Commun Nonlinear Sci Numer Simulat **17**, 2132 (2012).
[35] D. Borgogno, D. Grasso, F. Pegoraro, and T. Schep, Phys. Plasmas **18**, 102307 (2011).
[36] D. Borgogno, D. Grasso, F. Pegoraro, and T. Schep, Phys. Plasmas **18**, 102308 (2011).
[37] M. Hesse, T. Forbes, and J. Birn, Astrophys. Journal **631**, 1227 (2005).
[38] D. E. Wendel, D. K. Olson, M. Hesse, N. Aunai, M. Kuznetsova, H. Karimabadi, W. Daughton, and M. L. Adrian, Phys. Plasmas **20**, 122105 (2013).
[39] J. Egedal, A. Le, and W. Daughton, Phys. Plasmas **20**, 061201 (2013).
[40] C. E. Parnell, A. L. Haynes, and K. Galsgaard, J. Geophys. Res. **115**, A02102 (2010).
[41] E. G. Harris, Nuovo Cimento **23**, 115 (1962).
[42] V. Roytershteyn, W. Daughton, H. Karimabadi, and F. S. Mozer, Phys. Rev. Lett. **108**, 185001 (2012).
[43] P. Pritchett, F. Mozer, and M. Wilber, J. Geophys. Res. **117**, A06212 (2012).
[44] J. P. Eastwood, T. D. Phan, S. D. Bale, and A. Tjulin, Phys. Rev. Lett. **102**, 035001 (2009).
[45] O. Alexandrova, V. Carbone, P. Veltri, and L. Sorriso-Valvo, Astrophysical Journal **674**, 1153 (2008).
[46] F. Sahraoui, M. L. Goldstein, P. Robert, and Y. V. Khotyaintsev, Phys. Rev. Lett. **102**, 231102 (2009).
[47] H. Karimabadi, V. Roytershteyn, M. Wan, W. H. Matthaeus, W. Daughton, P. Wu, M. Shay, B. Loring, J. Borovsky, E. Leonardis, et al., Phys. Plasmas **20**, 012303 (2013).
[48] A. Rechester and M. Rosenbluth, Phys. Rev. Lett. **40**, 38 (1978), URL `http://link.aps.org/doi/10.1103/PhysRevLett.40.38`.
[49] See EPAPS Document No. E-PHPAEN-XX-XXXX for animations relevant to this paper. A direct link to this document may be found in the online article's HTML reference section. The document may also be reached via the EPAPS home-

page (http://www.aip.org/pubservs/epaps.html) or from ftp.aip.org in the directory /epaps. See the EPAPS homepage for more information. (????).
[50] W. Daughton, V. Roytershteyn, B. J. Albright, H. Karimabadi, L. Yin, and K. J. Bowers, Phys. Rev. Lett. **103**, 065004 (2009).
[51] M. Øieroset, T. D. Phan, J. P. Eastwood, M. Fujimoto, W. Daughton, M. Shay, V. Angelopoulos, F. S. Mozer, J. P. McFadden, D. E. Larson, et al., Phys. Rev. Lett. **107**, 165007 (2011).
[52] D. Fairfield, A. Otto, T. Mukai, S. Kokubun, R. P. Lepping, J. T. Steinberg, A. J. Lazarus, and T. Yamamoto, J. Geophys. Res. **105**, 21159 (2000).
[53] H. Hasegawa, M. Fujimoto, T.-D. Phan, H. Reme, A. Balogh, M. W. Dunlop, C. Hashimoto, and R. TanDokoro, Nature **430**, 755 (2004).
[54] Z. Y. Pu, M. Yan, and Z. X. Liu, J. Geophys. Res. **95**, 1055910566 (1990).
[55] K. Nykyri and A. Otto, Geophys. Res. Lett. **28**, 35653568 (2001).
[56] D. Knoll and L. Chacn, Phys. Rev. Lett. **88**, 215003 (2002).
[57] T. Nakamura, M. Fujimoto, and A. Otto, J. Geophys. Res. **113**, A09204 (2008).